frontiers in Materials

ORIGINAL RESEARCH
published: 07 September 2018
doi: 10.3389/fmats.2018.00053

Nonlinear Oxidation Behavior in Pure Ni and Ni-Containing Entropic Alloys

Songqin Xia[1,2,3], *Cláudio M. Lousada*[3], *Huahai Mao*[3,4], *Annika C. Maier*[5], *Pavel A. Korzhavyi*[3], *Rolf Sandström*[3], *Yugang Wang*[2] *and Yong Zhang*[1]*

[1] State Key Laboratory for Advanced Metals and Materials, University of Science and Technology Beijing, Beijing, China, [2] State Key Laboratory of Nuclear Physics and Technology, Peking University, Beijing, China, [3] Department of Materials Science and Engineering, KTH Royal Institute of Technology, Stockholm, Sweden, [4] Thermo-Calc Software AB, Solna, Sweden, [5] Department of Chemistry, Applied Physical Chemistry, KTH Royal Institute of Technology, Stockholm, Sweden

OPEN ACCESS

Edited by:
Gang Wang,
Shanghai University, China

Reviewed by:
Yiping Lu,
Dalian University of Technology (DUT), China
Zehra Canan Girgin,
Yildiz Technical University, Turkey
Run Rui Chen,
Harbin Institute of Technology, China

***Correspondence:**
Yong Zhang
drzhangy@ustb.edu.cn

Specialty section:
This article was submitted to Structural Materials, a section of the journal Frontiers in Materials

Received: *08 May 2018*
Accepted: *08 August 2018*
Published: *07 September 2018*

Citation:
Xia S, Lousada CM, Mao H, Maier AC, Korzhavyi PA, Sandström R, Wang Y and Zhang Y (2018) Nonlinear Oxidation Behavior in Pure Ni and Ni-Containing Entropic Alloys. Front. Mater. 5:53. doi: 10.3389/fmats.2018.00053

We performed a combined experimental and theoretical investigation of the oxidation behavior of pure Ni and of the following multi-component Ni-containing alloys with nearly equiatomic compositions: FeNi, CoFeNi, CoCrFeNi, and CoCrFeMnNi. The materials were exposed to air at ambient pressure and at a temperature of 800°C for 150 min, their weight-gain due to oxidation was continuously monitored and the products of oxidation were subsequently characterized by XRD. The most common oxides formed have spinel or halite structure and the materials resistance to oxidation increases as: FeNi < CoFeNi < Ni < CoCrFeMnNi < CoCrFeNi. We found further that the oxidation-resistance of the materials does not correlate linearly with the number of elements present, instead the type of elements impacts significantly the materials susceptibility to oxidative damage. Cr is the element that imparted higher resistance to oxidation while Mn and Fe worsened the materials performance. In order to better understand the mechanisms of oxidation we employed thermodynamic equilibrium calculations and predicted the phase stability of oxides of the elements that are present in the materials, in different ranges of temperature, composition and oxygen activity. Additionally, we determined the phase compositions for the thermodynamically stable oxides at 800°C. The results from the thermodynamic modeling are in good agreement with the experimental finds. The alloys with low resistance to oxidation such as CoFeNi and FeNi, form the Fe_3O_4 spinel phase which tends to dominate the phase diagram for these materials. The presence of Cr increases the resistance to atomic rearrangement due to slow diffusion in the complex structure of Cr containing spinel phases. This causes the extremely high resistance to oxidation of the CoCrFeNi alloy. The presence of Mn in CoCrFeNi stabilizes the Mn_3O_4 spinel, which reduces the oxidation-resistance of the alloys due to the high mobility of Mn.

Keywords: single-phase multicomponent alloys, oxidation, thermodynamic calculations, high-entropy alloys, nonlinear behavior

INTRODUCTION

Single-phase concentrated solid solution alloys, including high-entropy alloys (HEAs), have attracted wide interest in materials science due to their superior mechanical properties and stability at high temperature (Senkov et al., 2011; Zou et al., 2015). One important factor for the performance of the HEAs is the high entropy effect (Xia et al., 2017a). Even for a process with a positive change in enthalpy (ΔH), the change in Gibbs free energy (ΔG) can become negative at high temperatures because of the contribution of the entropy term ($-T\cdot\Delta S$) (Zhang et al., 2014, 2018). As a result, the high configurational entropy of HEAs can favor the formation and stability of a single phase and restrain the formation of intermetallic compounds with simple phases such as body-centered cubic (bcc), face-centered cubic (fcc), or hexagonal close-packed (hcp) (Gao, 2006). In addition to the unique mechanical properties (Xia et al., 2017b) and the wide temperature range of applications (Gludovatz et al., 2014), the increased resistance to radiation damage (Nagase et al., 2015; Xia et al., 2015) is another interesting feature of HEAs. Increasing the number of elements or increasing the structural complexity of HEAs is an effective way to improve their radiation resistance. For example, among Ni and the single-phase fcc concentrated solid solution alloys: FeNi, CoFeNi, CoCrFeNi and CoCrFeMnNi, the CoCrFeMnNi HEA shows the highest tendency for point defect recombination under irradiation (Lu et al., 2016). Also, Jin et al. reported that the volume swelling was reduced when the number of elements was increased and the CoCrFeMnNi HEA shows the best swelling resistance when compared to other alloys (Jin et al., 2016). Additionally, as reported by Wang et al. (2017b), the thermal vacancy equilibrium concentration was significantly enhanced by increasing the number of elements in HEAs. It has been suggested that the improved radiation resistance is correlated with increased complexity when going from pure Ni to more complex alloys that are single-phase solid solutions (Zhang et al., 2015; Zhao et al., 2017). These works demonstrate that controlling the composition of these alloys can significantly improve their irradiation performance. This makes them promising candidates for structural materials in nuclear reactors.

The best performing high entropy alloys are not always those with the highest number of elements and because of this HEAs are often designated "nonlinear alloys" (Miracle, 2017). A considerable number of investigations has shown that the mechanical performance of HEAs has little or no dependence on the number of elements present in equiatomic ratios (Wu et al., 2014). It has been demonstrated further that for the successful design of multicomponent alloys with improved properties more parameters than only an increase in entropy have to be considered (Yao et al., 2014; Deng et al., 2015). At present there is no knowledge on how the composition affects the high-temperature oxidation behavior of pure Ni and Ni-containing multi-component alloys of elements with equimolar ratios and their high-temperature oxidation behavior may also be nonlinear with regard to the number of constituents (Holcomb et al., 2015). For example the presence of Mn in HEA does not improve the oxidation resistance because Mn has a higher mobility than many other elements. This is also the main reason why most heat resistant commercial stainless steels and superalloys have a relatively low content of Mn. For example, high temperature Ni-based superalloys have a maximum specified level of Mn of approximately 0.5 wt% (Young, 2008).

The high-temperature oxidation behavior of HEAs is a relatively new and important topic and so far only a few studies on oxidation and corrosion of HEAs have been performed (Huang et al., 2004; Tsai et al., 2011; Senkov et al., 2012; Butler et al., 2015; Gorr et al., 2015, 2016; Holcomb et al., 2015; Liu et al., 2015; Butler and Weaver, 2016; Laplanche et al., 2016; Dabrowa et al., 2017). Here we report a study of the high-temperature oxidation behavior of Ni, FeNi, CoFeNi, CoCrFeNi, and CoCrFeMnNi. We aimed at assessing the effect of elemental composition in the oxidation kinetics and products formed. For this we have chosen materials that contain elements that typically facilitate the oxidation, such as Mn, and elements that typically increase the oxidation resistance, such as Cr. We found that CoCrFeNi has the highest resistance to oxidation and overall the presence of Cr tends to increase the materials resistance to oxidation. As observed for other systems the presence of Mn has a detrimental effect in the oxidation resistance of the materials.

MATERIALS AND METHODS

Ni, and its alloys FeNi, CoFeNi, CoCrFeNi, and CoCrFeMnNi, were synthesized as ingots with sizes of approximately Φ 40 mm $\times$ 10 mm via the arc-melting method starting from elements of high chemical purity (>99.99%) on a water-cooled copper hearth under an inert high-purity argon atmosphere. In order to ensure the chemical homogeneity of the samples, each ingot was flipped and re-melted four times. The ingots were then cut into 2 mm thick discs using electrical discharge machining. Thereafter, samples with sizes of 5 $\times$ 5 $\times$ 2 mm were cut with a diamond cutting wheel. Each sample was ground and polished with 0.6 mm diamond paste at the last polishing step according to the standard procedure.

Following polishing, the samples were dissolved and the stoichiometry of the alloys was determined using the technique of inductively coupled plasma atomic emission spectrometry (ICP-AES) with a Thermo Fisher iCAP 6000 instrument. For this, 100 mg of each alloy was dissolved in a mixture of hydrochloric and nitric acid (volume ratio 3:1). The resulting highly concentrated solutions were diluted 2,000 times with purified water (18.2 MOhm.cm, Merck MilliQ). In the ICP-AES measurements, the concentrations of Co, Cr, Fe, Mn, and Ni were determined at three different wavelengths for each element and the average of these three values was used for data evaluation.

Imaging of surface morphology and chemical analysis on the metals before oxidation were also performed using a scanning electron microscope (SEM) equipped with energy dispersive X-ray spectrometer (EDS).

Before the oxidation tests the specimens were ground to a 1,200 grit surface finish using SiC paper, cleaned with alcohol, dried and then stored in a two-neck glass vial under inert argon atmosphere. In order to obtain the weight-gain per unit surface

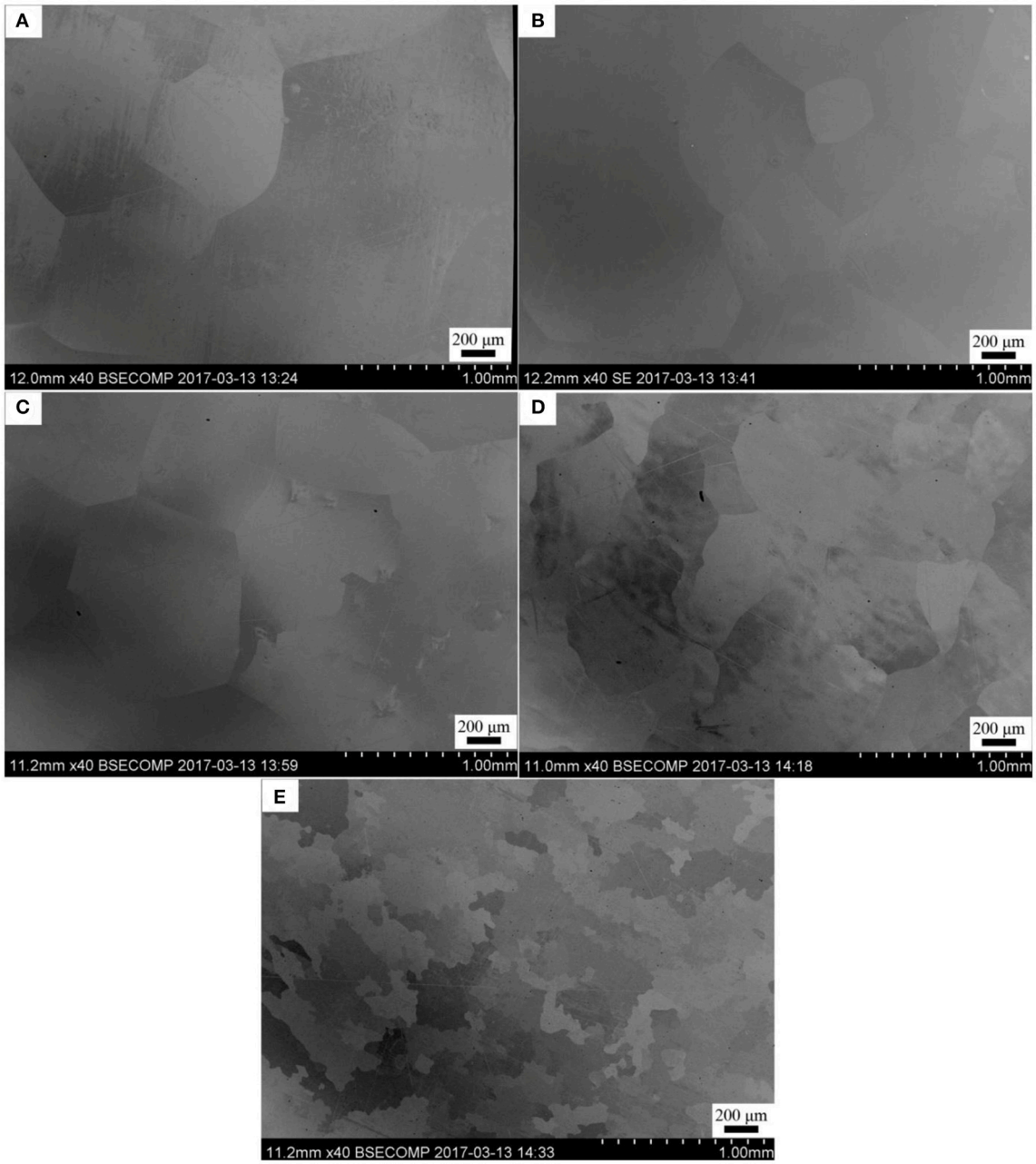

FIGURE 1 | BSE-images of: **(A)** pure Ni, **(B)** FeNi, **(C)** CoCrFe, **(D)** CoCrFeNi, and **(E)** CoCrFeMnNi alloys.

area ($\Delta W/A$) due to oxidation, we employed the geometrical surface areas of the samples, that were determined with a Vernier caliper. One disadvantage of this method is that it neglects the eventual surface roughness and porosity.

The oxidation of the samples was performed with a controlled air flow and the weight-gains recorded continuously as a function of time using a thermobalance TGA-TA Instruments Discovery TG in which the specimens were held in a platinum pan. The specimens were placed in the TGA instrument chamber at room temperature and the temperature was increased rapidly to that of the isothermal oxidation, 800°C, in order to minimize the oxidation during the process of heating.

For the comparison between the phases of the oxides as predicted by the thermodynamic modeling and those obtained in the oxidation experiments, we simulated the diffractograms of the oxide phases predicted by the thermodynamic modeling and compared with those obtained in the experiments. XRD measurements were performed in air at room temperature. The patterns were recorded with a PANalytical X'Pert PRO diffractometer using Cu Kα radiation ($\lambda = 1.5418$ Å) and

Bragg–Brentano geometry in the 2θ range from 10° to 100°. The simulations of the diffractograms were done with Rietveld refinements with RIETAN-FP (Izumi and Momma, 2007).

Thermodynamic calculations were performed using combined databases, the latest versions of TCHEA (Chen et al., 2017; Mao et al., 2017) and TCNI (Bratberg et al., 2012), from the Thermo-Calc Software package (Andersson et al., 2002). The databases are developed based on the CALPHAD approach, which couples phase diagram information and thermochemical properties. In the present study, equilibrium phase relations were calculated at various temperatures and oxygen contents for different metal systems. The phase equilibria at 800°C were further determined for varying oxygen activities.

RESULTS AND DISCUSSION

Structural, Microstructural and Chemical Analysis

The microstructure of the alloys after polishing and prior to oxidation are shown in **Figure 1.** It can be seen from the SEM images that all alloys exhibit a coarse equiaxed grain structure with sizes of several hundred micrometers or larger. Additionally, small pores with average sizes of around 10 μm can be seen in the multicomponent materials. The number of pores (or the total area occupied by pores) tends to increase with the number of components in the alloys except for FeNi. However, even for the most extreme case (CoCrFeMnNi), the fraction of the area occupied by the pores is small and therefore will have a negligible effect on the diffusion of gaseous oxygen and on the oxidation kinetics. The X-ray diffractograms (see section Structures of the Oxides) show that the alloys have a fcc structure.

The stoichiometries of the materials are given in **Table 1**. It can be seen that for three of the four multicomponent materials there are slight deviations from an equiatomic composition. The material with the largest deviation is CoFeNi and the material with the composition closest to equiatomic is CoCrFeNi. Nevertheless, for all alloys, the deviations from equiatomic compositions are small, which shows that our synthesis method is accurate.

TABLE 1 | Composition of the alloys used in this work.

Alloys	Elements	at.%	wt.%	Atomic ratio
CoCrFeMnNi	Co	20.77	21.82	$Co_{21}Cr_{20}Fe_{20}Mn_{19}Ni_{20}$
	Cr	20.13	18.66	
	Fe	20.35	20.26	
	Mn	18.65	18.26	
	Ni	20.10	21.02	
CoCrFeNi	Co	25.54	26.69	$Co_{25}Cr_{25}Fe_{25}Ni_{25}$
	Cr	24.75	22.82	
	Fe	24.91	24.67	
	Ni	24.80	25.82	
CoFeNi	Co	33.87	34.52	$Co_{34}Fe_{33}Ni_{33}$
	Fe	33.27	32.13	
	Ni	32.86	33.35	
FeNi	Fe	49.85	48.61	$Fe_{50}Ni_{50}$
	Ni	50.15	51.39	
Pure Ni	Ni	–	–	Ni

Oxidation Kinetics

The oxidation kinetics of the materials at $T = 800°C$ are shown in **Figure 2**, where the weight gain per unit surface area ($\Delta W/A$) is plotted as a function of oxidation time t. CoCrFeNi has the highest resistance to oxidation with a very small mass gain close to that of the detection limit of the instrument, while FeNi has the lowest resistance to oxidation. For pure Ni, CoFeNi, and CoCrFeMnNi, there were no obvious irregularities or fast changes in the slopes of the curves which indicates the absence of spalling. In order to quantify the oxidation rates, we plotted the logarithm of the weight gain per unit surface area, $\Delta W/A$, vs. logarithm of time, which revealed the parabolic oxidation behavior (slope = 0.5), which is shown in **Figure 3**. Therefore, the values of $\Delta W/A$ were analyzed in terms of parabolic kinetics with the parabolic rate constant (k_p) defined by Equation 1 according to the work of Holcomb (Holcomb et al., 2015).

$$k_p = \frac{(\frac{\Delta W}{A})^2}{2t} \quad (1)$$

The log (k_p) data is given in **Table 2** together with the goodness of the fit (R^2) of the data to Equation 1. It should be noted that the obtained log (k_p) value for the CoCrFeMnNi alloy is $-11.52\ g^2/cm^4/s$, which is in good agreement with the previously reported value by Laplanche et al. (2016), $-10.78\ g^2/cm^4/s$. Meanwhile, the mixing entropy dependence of oxidation resistance is shown in **Figure 4**. It can be shown that the presence of more alloying elements does not necessarily increase the oxidation resistance. This suggests nonlinear oxidation behavior in the multi-component alloys here studied. The results of log (k_p), show that the oxidation rate of CoCrFeNi is the lowest among all materials studied. This demonstrates that this material has the highest resistance to oxidation. It should be noted that the low R^2 value for CoCrFeNi alloy is due to the very small mass changes during oxidation which are close to the detection limit (0.01 mg) of the TGA instrument and as such suffer from larger uncertainties.

Thermodynamic Calculations

In this as well as the following paragraphs the authors refer to phases such as halite, spinel, corundum etc. It thereby solely referred to the structure type and not the respective mineral. **Figure 5** shows the equilibrium phase relations of various metals-oxygen isopleths. In the Ni-O system (**Figure 5A**) the metallic FCC phase is in equilibrium with halite in the full range of temperatures, while halite is the only oxide in contact with the (O_2) gas phase. In this case FCC_L12 represents the disordered FCC (Ni) phase, while HALITE represents NiO. In the FeNi-O system (**Figure 5B**) the FCC_L12 represents the disordered FCC (Fe, Ni), HALITE (Fe, Ni)O, and SPINEL stands for magnetite Fe_3O_4 with limited Ni solubility. The SPINEL phase is stable

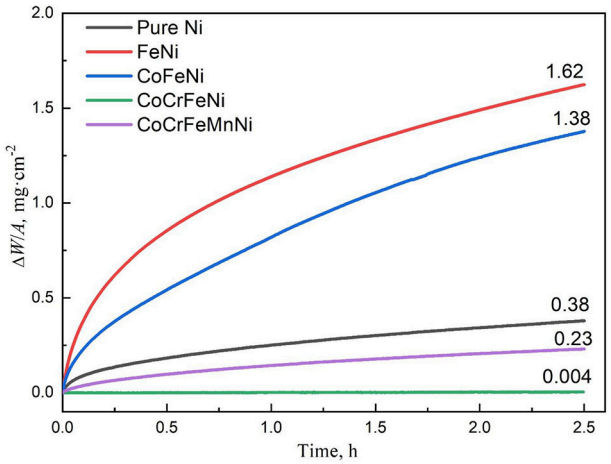

FIGURE 2 | Weight gain per unit surface area ($\Delta W/A$) as a function of oxidation time for pure Ni and other studied alloys after isothermal oxidation testing at 800°C for 150 min.

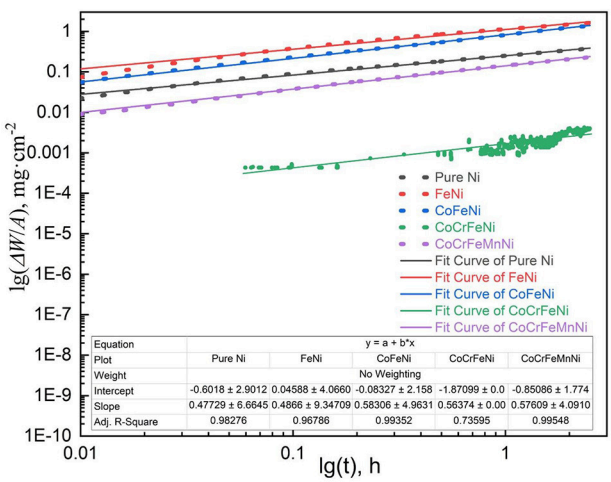

FIGURE 3 | The logarithm of the weight gain per unit surface area, $\Delta W/A$, vs. logarithm of time.

in wide temperature and O-content ranges. The gas phase is in equilibrium with both HALITE and SPINEL. In the CoFeNi-O system (**Figure 5C**) FCC_L12 represents the disordered FCC (Co, Fe, Ni). The FeO HALITE with a small amount of Co is stable in a wide temperature range and in the whole range of mole fractions of oxygen studied. The magnetite Fe_3O_4 is denoted as SPINEL, while the new phase, SPINEL#2, in this case stands for the Co_3O_4 spinel with Fe impurities. With increasing mole fraction of oxygen, O_2 gas is in equilibrium with HALITE and both SPINEL phases. In the CoCrFeNi-O system (**Figure 5D**) FCC_L12 represents the disordered FCC (Co, Cr, Fe, Ni) and this is in equilibrium with the Cr_2O_3 CORUNDUM phase in the full temperature range. At low temperatures there is an additional ordered BCC (B2) phase that coexists with FCC. At high mole fraction of oxygen the stable oxides are the HALITE

TABLE 2 | log k_p of the alloys oxidized in air at 800°C.

Alloys	log k_p ($g^2/cm^4/s$)	R^2
Pure Ni	−11.11	0.99884
FeNi	−9.85	0.99075
CoFeNi	−9.95	0.99731
CoCrFeNi	−15.05	0.76835
CoCrFeMnNi	−11.52	0.99979

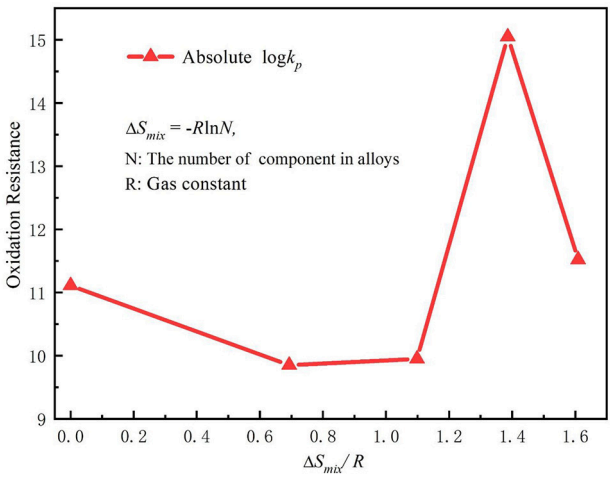

FIGURE 4 | The oxidation resistance as a function of the mixing entropy.

and SPINEL phases. It is worth mentioning that both SPINEL phases have the ability of accommodating large amounts of Cr. In the CoCrFeMnNi-O system (**Figure 5E**) FCC_L12 represents the disordered FCC (Co, Cr, Fe, Mn, and Ni). The SPINEL Mn3O4 that provides considerable solubility for Cr and Fe, is stable in wide ranges of both temperature and O composition. The ordered B2 phase appears at low temperatures.

In order to understand the oxidation mechanism and the products at 800°C, the dependency of the chemical activity of O with the overall O molar fraction was calculated using the CALPHAD-type thermodynamic databases. The results are shown in **Figure 6**. For the oxidation of pure Ni, **Figure 6A**, there is only one oxide namely HALITE i.e., $(Ni^{+2})_1(O^{-2})_1$ at high O activity. For the oxidation of the FeNi alloy, see **Figure 6B**, both oxides with the structure of HALITE and SPINEL tend to be in equilibrium with O_2 gas. According to our calculations, the HALITE is mainly NiO with Fe solubility in the formulae of $(Ni^{+2}, Fe^{+2})_1(O^{-2})_1$, while the SPINEL is mainly Fe_3O_4 with dissolved Ni as $(Fe^{+3})_1(Fe^{+3}, Ni^{+2})_2(O^{-2})_4$ i.e., an inverse spinel. For the oxidation of the CoFeNi alloy, see **Figure 6C**, there is a second SPINEL phase in addition of the HALITE and SPINEL. The corresponding phase constitutions are predicted to be: $(Ni^{+2},Co^{+2},Fe^{+2})_1(O^{-2})_1$ for HALITE, $(Fe^{+3})_1(Ni^{+2},Fe^{+3},Co^{+3})_2(O^{-2})_4$ for the inverse SPINEL, and $(Co^{+2},Co^{+3},Fe^{+3})_1(Co^{+3},Fe^{+3},Co^{+2})_2(O^{-2})_4$ for the normal SPINEL#2. For the oxidation of the CoCrFeNi alloy,

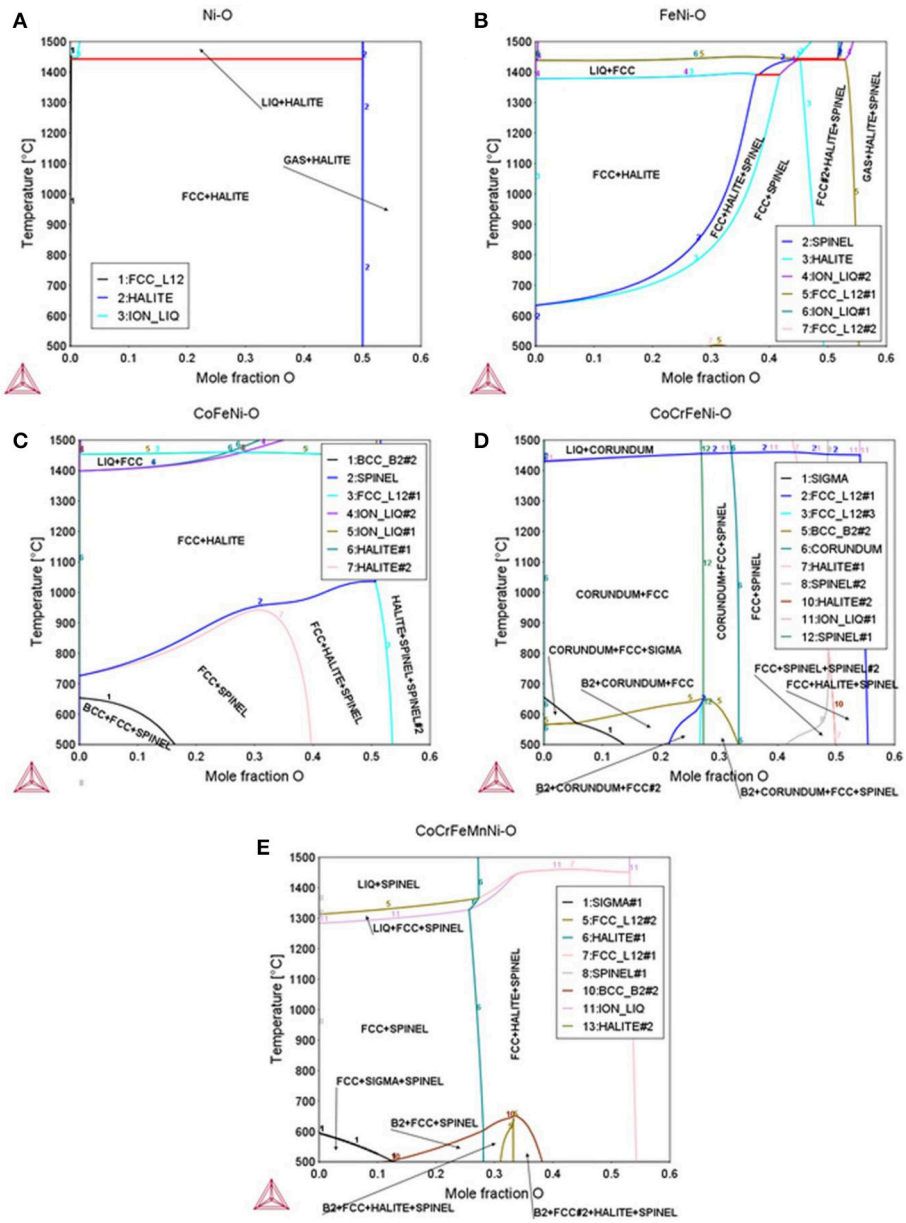

FIGURE 5 | Calculated equilibrium phase relations of metals-oxygen isopleths **(A)** Ni-O; **(B)** FeNi-O; **(C)** CoFeNi-O; **(D)** CoCrFeNi-O; **(E)** CoCrFeMnNi-O.

see **Figure 6D**, the stable oxides are the same as that of the CoFeNi-O system, i.e., HALITE+SPINEL+SPINEL#2. However, with the presence of Cr in the system, the composition of the SPINEL phases become $(Fe^{+3})_1(Ni^{+2},Fe^{+3},Cr^{+3})_2(O^{-2})_4$ for the inverse SPINEL and $(Co^{+2},Fe^{+3})_1(Cr^{+3},Fe^{+3},Co^{+2})_2(O^{-2})_4$ for the normal SPINEL#2. For the oxidation of the CoCrFeMnNi alloy, see **Figure 6E**, the two SPINEL phases are the most stable oxides at high O activities. Our calculations show that most of Mn constitutes the inverse SPINEL with the formulae $(Fe^{+3},Mn^{+2})_1(Ni^{+2},Mn^{+4},Mn^{+3})_2(O^{-2})_4$, while a minor amount is present in the normal SPINEL#2 $(Co^{+2},Fe^{+3})_1(Cr^{+3},Mn^{+3},Co^{+2})_2(O^{-2})_4$.

Structures of the Oxides

In order to identify the crystal structures of the oxides formed in the oxidation experiments a characterization with XRD was performed. To unequivocally assign the oxide peaks in the diffractograms, the unoxidized specimens and the sample-holders were also characterized by XRD. The measured diffractograms of the oxides on the oxidized samples were then compared with simulated diffractograms of the oxides predicted in the thermodynamic modeling reported in the previous section, as shown in **Figures 7A–E**.

Figures 8B–F show the room-temperature XRD patterns of the materials before and after oxidation at 800°C for 150 min.

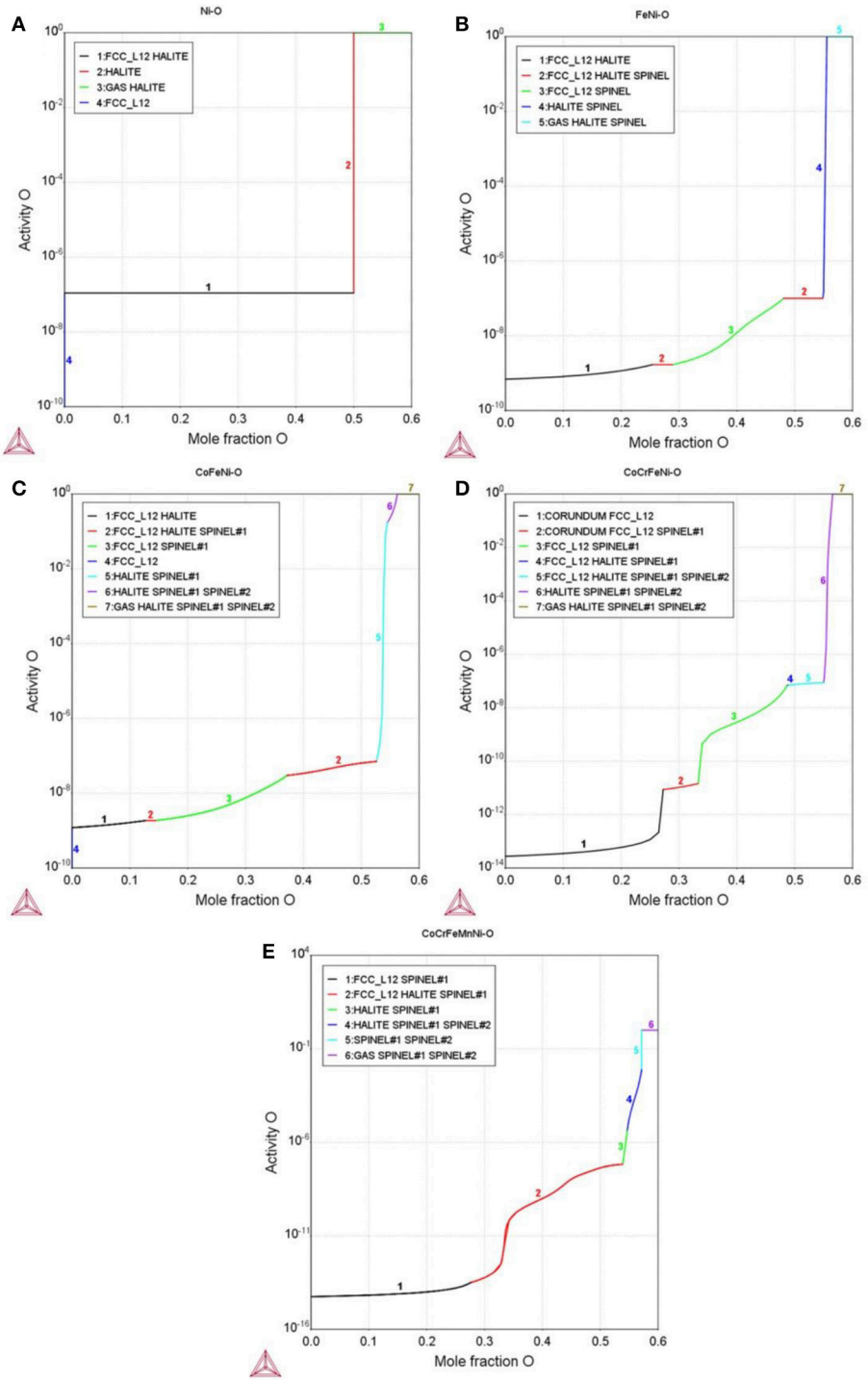

FIGURE 6 | Calculated oxygen activity corresponds to various phase equilibria at 800°C for the oxidation of different metal systems. The reference state is the gas phase at this temperature. **(A)** Ni-O; **(B)** FeNi-O; **(C)** CoFeNi-O; **(D)** CoCrFeNi-O; **(E)** CoCrFeMnNi-O.

Besides, the XRD pattern of the sample holder is given, as shown in **Figure 8A**. It can be seen that all unoxidized materials have a single fcc solid-solution phase (Wu et al., 2014). The peaks at ∼ 79.0 degrees visible in all diffractograms are due to the sample-holder and not to the materials being studied. For the oxide formed in the pure Ni sample, all peaks correspond to NiO with halite structure (Yue and Zhou, 2007), with the exceptions of the peak at 52 degrees with high intensity and the peak at 44.7°

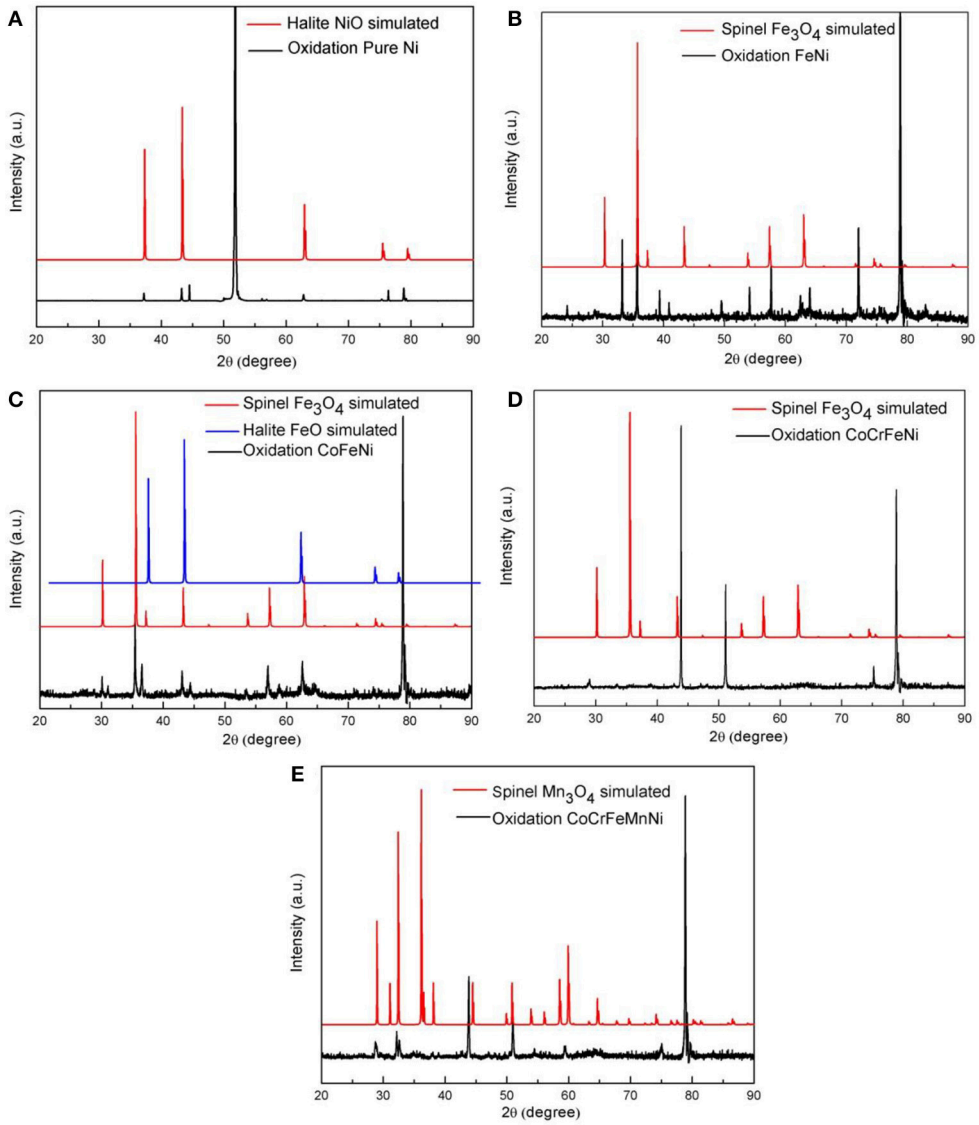

FIGURE 7 | The comparison between the diffractograms of the oxides formed in the oxidation experiments and the simulated diffractograms of the oxides predicted by Calphad modeling. **(A)** Ni-O; **(B)** FeNi-O; **(C)** CoFeNi-O; **(D)** CoCrFeNi-O; **(E)** CoCrFeMnNi-O.

that corresponds to the fcc-Ni substrate (Ogata et al., 2002) as shown in **Figure 8B**. For FeNi, the products of oxidation consist mainly of iron-rich oxides with spinel-Fe3O4 and α-Fe2O3, the peaks at 24.0, 33.1, 35.6, 40.8, 49.4, 54.0, 62.4, and 63.9 in the XRD pattern of α-Fe2O3 indicate the presence of the hematite phase (Kittel, 2005), while the pattern of Fe3O4 shows peaks at 30.1, 35.6, 43.3, 57.1, and 62.8 corresponding to the magnetite phase (Tian et al., 2005). These results agree well with previously reported work by Saiphaneendra et al. (2017). For CoFeNi, the higher intensity peaks reveal that the oxide contains mainly the Fe3O4 (spinel) phase while the peaks with lower intensities reveal the presence of FeO (**Figure 8D**). For the CoCrFeNi alloys (**Figure 8E**), the diffractogram obtained after oxidation is still dominated by the peaks of the CoCrFeNi alloy which is consistent with the low mass gain during oxidation and confirms the high resistance of the material to oxidation. For CoCrFeMnNi, the oxide formed consists of Mn3O4 with Hausmannite phase which is in agreement with a previously obtained result for this alloy at 900°C in air (Laplanche et al., 2016). For both CoCrFeNi and CoCrFeMnNi, the XRD patterns obtained after isothermal oxidation show one peak at ∼30 degrees, which appears to correspond to the ordered phase with B2 structure (Xia et al., 2015; Wang et al., 2017a), however, further experiments are needed in order to confirm this observation.

Oxidation Mechanism

The thermodynamic calculations show that for pure Ni metal, the halite structure of NiO is the only stable oxide and this

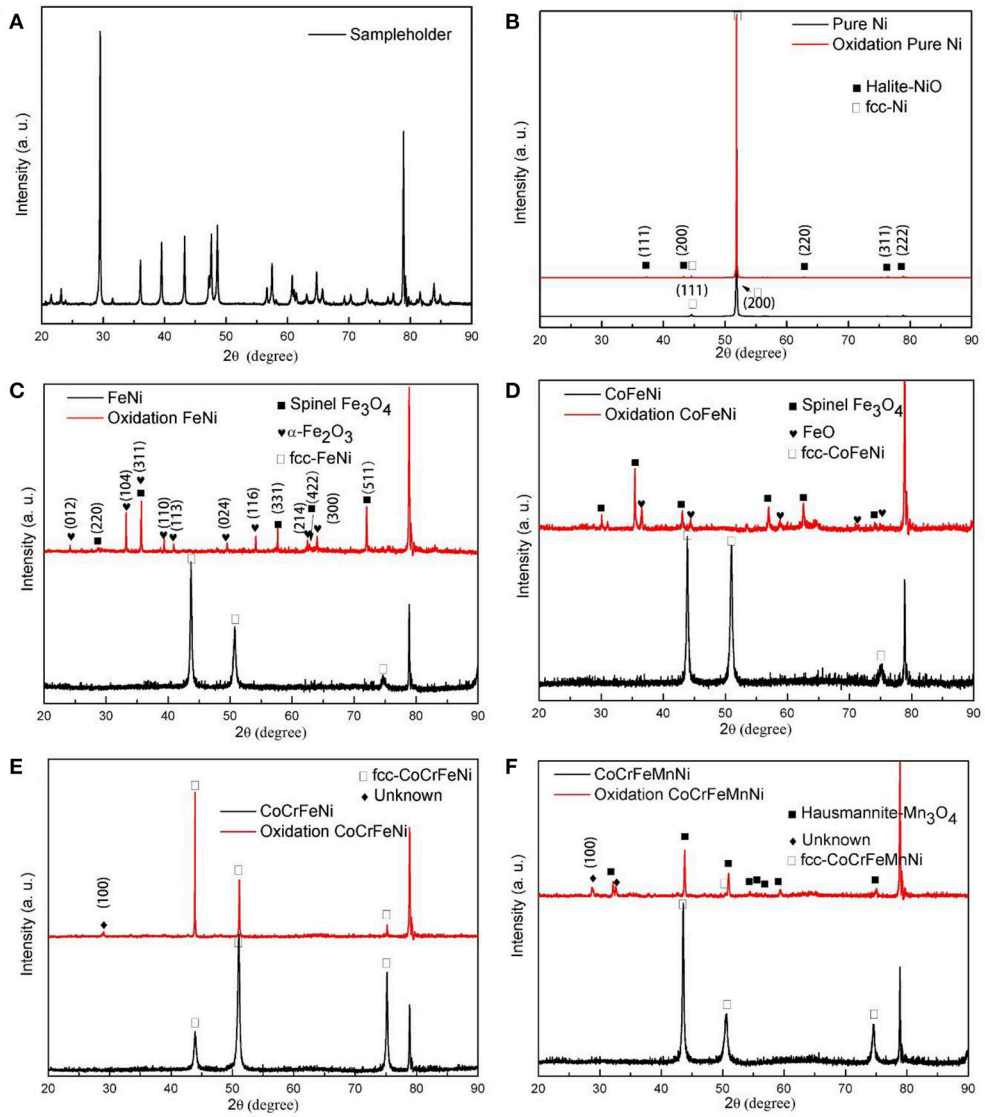

FIGURE 8 | XRD patterns on the pure Ni and other studied alloys at 800°C for 150 min. **(A)** Sample holder; **(B)** Pure Ni; **(C)** FeNi; **(D)** CoFeNi; **(E)** CoCrFeNi; **(F)** CoCrFeMnNi.

product has not been observed in the experiments. For NiFe the oxide Fe_3O_4 with spinel structure is observed in the experiments but has not been predicted in the thermodynamic modeling. This discrepancy between the experiments and calculations has origin in the fact that the oxidation is largely a kinetic process and some oxidation products do not correspond to a global equilibrium. When the metal is in contact with gas, both halite and spinel products tend to form through the diffusion of O-atoms into the metal (while a number of metal atoms will migrate toward the surface). As long as sufficient O enters the interstitial sites of the Fe FCC lattice, the Fe_3O_4 spinel crystallizes through nucleation and grows. The rather open structure of Fe_3O_4 can locally accommodate an extra amount of O yielding the new Fe_2O_3 phase. At the same time the growth of Fe_2O_3 suppresses the formation of halite. The appearance of Fe_2O_3 and the absence of halite can probably be attributed to a local equilibrium in the oxidation experiments. With the addition of Co to the system, the oxidation products of CoFeNi observed in the experiments are the spinel and halite, which agrees well with the predictions of the calculations. It should be mentioned that the calculations also predict the existence of a second spinel phase. This is mainly the normal Co_3O_4 spinel with a small amount of dissolved Fe, and the inverse Fe_3O_4 spinel phase with considerable amounts of dissolved Ni and Co. The presence of Ni and Co in the spinel phase makes the formation of Fe_2O_3 unfavorable. This indicates that the oxidation kinetics in the CoFeNi are slower than those in the FeNi alloy which can be due to the increased composition complexity and/or configurational entropy. This observation seems to be supported by the fact that the best oxidation resistance alloy is the

CoCrFeNi. Moreover, a detailed thermodynamic calculation on the oxidation of CoCrFeNi revealed an extensive involvement of Cr in the spinel phases. The coupling of the complex constitution of the spinel phase and the slow diffusion of Cr in the complex FCC CoCrFeNi matrix contributes to high oxidation-resistance of the CoCrFeNi alloy. However, adding Mn to this alloy changes the composition of the formed spinel phase to almost solely Mn_3O_4. The relatively simple composition of the oxide in the CoCrFeMnNi system compared to that in CoCrFeNi, plus the faster diffusion of Mn, results in the formation of Mn_3O_4 spinel and in the oxidation of the CoCrFeMnNi alloy.

In the XRD patterns for CoCrFeNi and CoCrFeMnNi shown in **Figures 7E,F**, besides the peaks corresponding to the oxides there is one unknown peak. This could be related with the metallic B2 phase. This phase was predicted as being stable in these systems at temperatures slightly lower than 800°C. A minor amount of B2 could be readily formed during the heating and oxidation due to the semi-coherency of B2 and FCC matrix.

CONCLUSIONS

The oxidation behavior of pure Ni and the four Ni-containing high entropy alloys: FeNi, CoFeNi, CoCrFeNi, and CoCrFeMnNi was investigated with a combined experimental-thermodynamic modeling approach. Our results show that for the oxidation at 800°C caused by air, the number of elements in the alloys does not lead directly to higher oxidation resistance. Instead, the type of elements present in the materials largely determines their performance. The resistance to oxidation increases in the order FeNi < CoFeNi < Ni < CoCrFeMnNi < CoCrFeNi. The highest oxidation resistance has been obtained for the Cr containing alloys, while the alloys FeNi and CoFeNi are those that oxidize faster. Overall we found that the presence of Cr improves the resistance to oxidation of the alloys while the presence of Mn and Fe is detrimental. From these two elements Mn is the one that has a more negative impact on the materials performance. These phenomena are related with the type of oxides that are formed in the oxidation of the materials. The formation of oxides where diffusion of metal atoms is faster leads to a lower resistance to oxidation and vice versa. The analysis of the plots of the parabolic rate constants for oxidation shows that the rate of oxidation of CoCrFeNi is the lowest which indicates that the activation energy for the oxidation of this material may be the highest among all the materials here studied.

Our study suggests that for applications in oxidizing environments at high temperatures, equimolar alloys should contain Cr and the presence of Mn should be avoided.

AUTHOR CONTRIBUTIONS

SX, CL, HM, AM, PK, RS, and YW carried out the experiments and wrote the paper. YZ design the experiments and reviewed and revised the paper, all the authors joined discussion about the paper.

ACKNOWLEDGMENTS

The Carl Tryggers Stiftelse för Vetenskaplig Forskning is gratefully acknowledged for financial support. SX would like to acknowledge the China Scholarship Council. YZ appreciates the financial support from the National Science Foundation of China (Nos. 51471025 and 51671020).

REFERENCES

Andersson, J. O., Helander, T., Höglund, L., Shi, P., and Sundman, B. (2002). Thermo-Calc & DICTRA, computational tools for materials science. *Calphad* 26, 273–312. doi: 10.1016/S0364-5916(02)00037-8

Bratberg, J., Mao, H., Kjellqvist, L., Engström, A., Mason, P., and Chen, Q. (2012). The development and validation of a new thermodynamic database for Ni-based alloys. *Superalloys* 12, 803–812. doi: 10.1002/9781118359259.ch50

Butler, T. M., Alfano, J. P., Martens, R. L., and Weaver, M. L. (2015). High-temperature oxidation behavior of Al-Co-Cr-Ni-(Fe or Si) multicomponent high-entropy alloys. *JOM* 67, 246–259. doi: 10.1007/s11837-014-1185-7

Butler, T. M., and Weaver, M. L. (2016). Oxidation behavior of arc melted AlCoCrFeNi multi-component high-entropy alloys. *J. Alloys Compd.* 674, 229–244. doi: 10.1016/j.jallcom.2016.02.257

Chen, H. L., Mao, H. H., and Chen, Q. (2017). Database development and Calphad calculations for high entropy alloys: challenges, strategies, and tips. *Mater. Chem. Phys.* 210, 279–290. doi: 10.1016/j.matchemphys.2017.07.082

Dabrowa, J., Cieślak, G., Stygar, M., Mroczka, K., Berent, K., Kulik, T., et al. (2017). Influence of Cu content on high temperature oxidation behavior of $AlCoCrCu_xFeNi$ high entropy alloys ($x = 0$; 0.5; 1). *Intermetallics* 84, 52–61. doi: 10.1016/j.intermet.2016.12.015

Deng, Y., Tasan, C. C., Pradeep, K. G., Springer, H., Kostka, A., and Raabe, D. (2015). Design of a twinning-induced plasticity high entropy alloy. *Acta Mater.* 94, 124–133. doi: 10.1016/j.actamat.2015.04.014

Gao, M. C. (2006). "Design of high-entropy alloys," in *High-Entropy Alloys: Fundamentals and Applications*, eds M. C. Gao, J. W. Yeh, P. K. Liaw, and Y. Zhang (Cham: Springer International Publishing), 369–398.

Gludovatz, B., Hohenwarter, A., Catoor, D., Chang, E. H., George, E. P., and Ritchie, R. O. (2014). A fracture-resistant high-entropy alloy for cryogenic applications. *Science* 345, 1153–1158. doi: 10.1126/science.1254581

Gorr, B., Azim, M., Christ, H. J., Mueller, T., Schliephake, D., and Heilmaier, M. (2015). Phase equilibria, microstructure, and high temperature oxidation resistance of novel refractory high-entropy alloys. *J. Alloys Compd.* 624, 270–278. doi: 10.1016/j.jallcom.2014.11.012

Gorr, B., Mueller, F., Christ, H. J., Mueller, T., Chen, H., Kauffmann, A., and Heilmaier, M. (2016). High temperature oxidation behavior of an equimolar refractory metal-based alloy 20Nb-20Mo-20Cr-20Ti-20Al with and without Si addition. *J. Alloys Compd.* 688, 468–477. doi: 10.1016/j.jallcom.2016.07.219

Holcomb, G. R., Tylczak, J., and Carney, C. (2015). Oxidation of CoCrFeMnNi high entropy alloys. *JOM* 67, 2326–2339. doi: 10.1007/s11837-015-1517-2

Huang, P. K., Yeh, J. W., Shun, T. T., and Chen, S. K. (2004). Multi-principal-element alloys with improved oxidation and wear resistance for thermal spray coating. *Adv. Eng. Mater.* 6, 74–78. doi: 10.1002/adem.200300507

Izumi, F., and Momma, K. (2007). Three-dimensional visualization in powder diffraction. *Solid State Phenom.* 130, 15–20. doi: 10.4028/www.scientific.net/SSP.130.15

Jin, K., Lu, C., Wang, L. M., Qu, J., Weber, W. J., Zhang, Y., and Bei, H. (2016). Effects of compositional complexity on the ion-irradiation induced swelling and hardening in Ni-containing equiatomic alloys. *Scripta Mater.* 119, 65–70. doi: 10.1016/j.scriptamat.2016.03.030

Kittel, C. (2005). *Introduction to Solid State Physics, 8th Edn*. Hoboken, NJ: John Wiley & Sons.

Laplanche, G., Volkert, U. F., Eggeler, G., and George, E. P. (2016). Oxidation behavior of the CrMnFeCoNi high-entropy Alloy. *Oxid. Met.* 85, 629–645. doi: 10.1007/s11085-016-9616-1

Liu, Y. X., Cheng, C. Q., Shang, J. L., Wang, R., Li, P., and Zhao, J. (2015). Oxidation behavior of high-entropy alloys $Al_xCoCrFeNi$ ($x = 0.15, 0.4$) in supercritical water and comparison with HR3C steel. *Trans. Nonferrous Met. Soc. China* 25, 1341–1351. doi: 10.1016/S1003-6326(15)63733-5

Lu, C. Y., Niu, L. L., Chen, N. J., Jin, K., Yang, T. N., Xiu, P. Y., et al. (2016). Enhancing radiation tolerance by controlling defect mobility and migration pathways in multicomponent single-phase alloys. *Nat. Commun.* 7:13564. doi: 10.1038/ncomms13564

Mao, H., Chen, H.-L., and Chen, Q. (2017). TCHEA1: a thermodynamic database not limited for "High Entropy" Alloys. *J. Phase Equilib. Diffus.* 38, 353–368. doi: 10.1007/s11669-017-0570-7

Miracle, D. B. (2017). High-entropy alloys: a current evaluation of founding ideas and core effects and exploring "Nonlinear Alloys." *JOM* 69, 2130–2136. doi: 10.1007/s11837-017-2527-z

Nagase, T., Rack, P. D., Noh, J. H., and Egami, T. (2015). *in-situ* TEM observation of structural changes in nano-crystalline CoCrCuFeNi multicomponent high-entropy alloy (HEA) under fast electron irradiation by high voltage electron microscopy (HVEM). *Intermetallics* 59, 32–42. doi: 10.16/j.intermet.2014.12.007

Ogata, S., Li, J., and Yip, S. (2002). Ideal pure shear strength of aluminum and copper. *Science* 298, 807–811. doi: 10.1126/science.1076652

Saiphaneendra, B., Saxena, T., Singh, S. A., Madras, G., and Srivastava, C. (2017). Synergistic effect of co-existence of hematite (α-Fe_2O_3) and magnetite (Fe_3O_4) nanoparticles on graphene sheet for dye adsorption. *J. Environ. Chem. Eng.* 5, 26–37. doi: 10.1016/j.jece.2016.11.017

Senkov, O., Senkova, S., Dimiduk, D., Woodward, C., and Miracle, D. (2012). Oxidation behavior of a refractory $NbCrMo_{0.5}Ta_{0.5}TiZr$ alloy. *J. Mater. Sci.* 47, 6522–6534. doi: 10.1007/s10853-012-6582-0

Senkov, O., Wilks, G., Scott, J., and Miracle, D. (2011). Mechanical properties of $Nb_{25}Mo_{25}Ta_{25}W_{25}$ and $V_{20}Nb_{20}Mo_{20}Ta_{20}W_{20}$ refractory high entropy alloys. *Intermetallics* 19, 698–706. doi: 10.1016/j.intermet.2011.01.004

Tian, C. S., Qian, D., Wu, D., He, R. H., Wu, Y. Z., Tang, W. X., et al. (2005). Body-centered-cubic Ni and its magnetic properties. *Phys. Rev. Lett.* 94:137210. doi: 10.1103/PhysRevLett.94.137210

Tsai, M. H., Wang, C. W., Tsai, C. W., Shen, W. J., Yeh, J. W., Gan, J. Y., and Wu, W. W. (2011). Thermal stability and performance of NbSiTaTiZr high-entropy alloy barrier for copper metallization. *J. Electrochem. Soc.* 158, H1161–H1165. doi: 10.1149/2.056111jes

Wang, J., Niu, S., Guo, T., Kou, H., and Li, J. (2017a). The FCC to BCC phase transformation kinetics in an $Al_{0.5}CoCrFeNi$ high entropy alloy. *J. Alloys Compd.* 710, 144–150. doi: 10.1016/j.jallcom.2017.03.249

Wang, Z. J., Liu, C. T., and Dou, P. (2017b). Thermodynamics of vacancies and clusters in high-entropy alloys. *Phys. Rev. Mater.* 1:043601. doi: 10.1103/PhysRevMaterials.1.043601

Wu, Z., Bei, H., Pharr, G. M., and George, E. P. (2014). Temperature dependence of the mechanical properties of equiatomic solid solution alloys with face-centered cubic crystal structures. *Acta Mater.* 81, 428–441. doi: 10.1016/j.actamat.2014.08.026

Xia, S., Yang, X., Chen, M., Yang, T., and Zhang, Y. (2017a). The Al effects of Co-free and V-containing high-entropy alloys. *Metals* 7:18. doi: 10.3390/met7010018

Xia, S. Q., Gao, M. C., and Zhang, Y. (2017b). Abnormal temperature dependence of impact toughness in $Al_xCoCrFeNi$ system high entropy alloys. *Mater. Chem. Phys.* 210, 213–221. doi: 10.1016/j.matchemphys.2017.06.021

Xia, S. Q., Yang, X., Yang, T. F., Liu, S., and Zhang, Y. (2015). Irradiation resistance in $Al_xCoCrFeNi$ high entropy Alloys. *JOM* 67, 2340–2344. doi: 10.1007/s11837-015-1568-4

Yao, M., Pradeep, K., Tasan, C., and Raabe, D. (2014). A novel, single phase, non-equiatomic FeMnNiCoCr high-entropy alloy with exceptional phase stability and tensile ductility. *Scripta Mater.* 72, 5–8. doi: 10.1016/j.scriptamat.2013.09.030

Young, D. J. (2008). *High Temperature Oxidation and Corrosion of Metals.* Amsterdam: Elsevier Science.

Yue, W., and Zhou, W. (2007). Porous crystals of cubic metal oxides templated by cage-containing mesoporous silica. *J. Mater. Chem.* 17, 4947–4952. doi: 10.1039/B709076E

Zhang, W. R., Liaw, P. K., and Zhang, Y. (2018). Science and technology in high-entropy alloys. *Sci. China Mater.* 61, 2–22. doi: 10.1007/s40843-017-9195-8

Zhang, Y., Stocks, G. M., Jin, K., Lu, C., Bei, H., Sales, B. C., et al. (2015). Influence of chemical disorder on energy dissipation and defect evolution in concentrated solid solution alloys. *Nat. Commun.* 6:8736. doi: 10.1038/ncomms9736

Zhang, Y., Zuo, T. T., Tang, Z., Gao, M. C., Dahmen, K. A., Liaw, P. K., et al. (2014). Microstructures and properties of high-entropy alloys. *Prog. Mater. Sci.* 61, 1–93. doi: 10.1016/j.pmatsci.2013.10.001

Zhao, S., Velisa, G., Xue, H., Bei, H., Weber, W. J., and Zhang, Y. (2017). Suppression of vacancy cluster growth in concentrated solid solution alloys. *Acta Mater.* 125, 231–237. doi: 10.1016/j.actamat.2016.11.050

Zou, Y., Ma, H., and Spolenak, R. (2015). Ultrastrong ductile and stable high-entropy alloys at small scales. *Nat. Commun.* 6:7748. doi: 10.1038/ncomms8748

Conflict of Interest Statement: The authors declare that the research was conducted in the absence of any commercial or financial relationships that could be construed as a potential conflict of interest.